Autonomous Palpation for Tumor Localization: Design of a Palpation Probe and Gaussian Process Adaptive Sampling

Animesh Garg
Ken Goldberg, Ed.
Pieter Abbeel, Ed.
Alper Atamturk, Ed.

Electrical Engineering and Computer Sciences
University of California at Berkeley

Technical Report No. UCB/EECS-2016-140
http://www.eecs.berkeley.edu/Pubs/TechRpts/2016/EECS-2016-140.html

August 11, 2016

Acknowledgement

I would like to thank Ken Goldberg for his advice, support, and encouragement. His experience and intuition in geometric planning were crucial to the development of contributions in this thesis.
I also express my gratitude towards Alper Atamturk and Pieter Abbeel for being on my masters' thesis committee and providing valuable feedback.
I would also like to thank all the co-authors for CASE 2016 and CASE 2015 paper for their input, and hard work that led to this thesis.

Autonomous Palpation for Tumor Localization:
Design of a Palpation Probe and Gaussian Process Adaptive Sampling

by

Animesh Garg

A thesis submitted in partial satisfaction of the
requirements for the degree of
Master of Science

in

Computer Science

in the

Graduate Division

of the

University of California, Berkeley

Committee in charge:

Professor Ken Goldberg, Chair
Professor Pieter Abbeel
Professor Alper Atamürk

Summer 2016

The thesis of Animesh Garg, titled Autonomous Palpation for Tumor Localization: Design of a Palpation Probe and Gaussian Process Adaptive Sampling, is approved:

Chair _____ Date _____

_____ Date _____

_____ Date _____

University of California, Berkeley

Autonomous Palpation for Tumor Localization:
Design of a Palpation Probe and Gaussian Process Adaptive Sampling

Abstract

Autonomous Palpation for Tumor Localization:
Design of a Palpation Probe and Gaussian Process Adaptive Sampling

by

Animesh Garg

Master of Science in Computer Science

University of California, Berkeley

Professor Ken Goldberg, Chair

In surgical tumor removal, inaccurate localization can lead to the removal of excessive healthy tissue and failure to completely remove cancerous tissue. Automated palpation with a tactile sensor has the potential to precisely estimate the geometry of embedded tumors during robot-assisted minimally invasive surgery (RMIS). This thesis is a step towards enabling autonomous palpation for tumor localization. Specifically, this thesis presents a novel, low-cost design for a palpation probe and a Bayesian algorithm using Gaussian Process Adaptive Sampling for tumor localization.

First, we describe the design and evaluation of the single-use palpation probe, which we call PALP, to localize subcutaneous blood vessels. It measures probe tip deflection using a Hall Effect sensor as the spherical tip is moved tangentially across a surface under automated control. The probe is intended to be single-use and disposable and fits on the end of an 8mm diameter needle driver in the Intuitive Surgical da Vinci® Research Kit (dVRK). We report experiments for quasi-static sliding palpation with silicone based tissue phantoms with subcutaneous blood vessel phantoms. We analyze the signal-to-noise ratios with varying size of blood vessels, subcutaneous depths, indentation depths and sliding speeds. We observe that the probe can detect phantoms of diameter 2.25 mm at a depth of up to 5 mm below the tissue surface.

Secondly, we address the use of our design for autonomous tumor localization. We formulate tumor boundary localization as a Bayesian optimization model along implicit curves overestimated tissue stiffness. We propose a Gaussian Process Adaptive Sampling algorithm called Implicit Level Set Upper Confidence Bound (ILS-UCB), that prioritizes sampling near a level set of the estimate. We compare ILS-UCB to two other palpation algorithms in simulated experiments with varying levels of measurement noise and bias. We find that ILS-UCB significantly outperforms the other two algorithms as measured by the symmetric difference between tumor boundary estimate and ground truth, reducing error by up to $10x$. Physical experiments with the PALP in a dVRK show that ILS-UCB can localize the tumor boundary with approximately the same accuracy as a dense raster scan while requiring $10x$ fewer measurements.

Contents

Contents **i**

1 Introduction to Tactile Tumor Localization **1**
1.1 Summary of Contributions 2
1.2 Background and Related Work 3

2 Design of a Disposable Palpation Probe **7**
2.1 Palpation Probe Design 7
2.2 System Design 9
2.3 Experimental evaluation of Palpation Probe 11
2.4 Discussion of Results 15

3 Guassian Process Adaptive Sampling **16**
3.1 Problem Statement 16
3.2 Gaussian Process Adaptive Sampling 17
3.3 Palpation Algorithms 18
3.4 Simulation Experiments 20
3.5 Physical Experiments 22

4 Future Work and Conclusion **26**

Bibliography **28**

Acknowledgments

I would like to thank Ken Goldberg for his advice, support, and encouragement. His experience and intuition in geometric planning were crucial to the development of contributions in this thesis.

I also express my gratitude towards Alper Atamtürk and Pieter Abbeel for being on my masters' thesis committee and providing valuable feedback.

I would also like to sincerely thank all the collaborators for their input, critique and hard work on the projects contributing to this thesis: Stephen McKinley, Lauren Miller, Siddarth Sen, Yiming Jen, Rishi Kapadia, Adithya Murali, Sachin Patil, Allison Okamura and Pieter Abbeel.

In particular, the work on palpation probe design was performed jointly with Stephen McKinley, during one of our first collaborations. And Lauren Miller closely assisted and advised during the development of the Gaussian Process Adaptive Sampling algorithms. I am deeply grateful to both of them and feel fortunate to have worked closely with them.

This research was performed with UC Berkeley's AUTOLAB under the UC Berkeley Center for Information Technology in the Interest of Society (CITRIS) "People and Robots" Initiative (robotics.citris-uc.org). I would also like to acknowledge the support from Intuitive Surgical for the robotic equipment grant. The authors on related papers were supported in part by the U.S. National Science Foundation under NRI Award IIS-1227536: Multilateral Manipulation by Human-Robot Collaborative Systems, by Google, Cisco, by a major equipment grant from Intuitive Surgical, and by generous donations from Andy Chou and Susan and Deepak Lim.

Chapter 1

Introduction to Tactile Tumor Localization

This thesis presents a novel, low-cost palpation probe design for use in Robot-Assisted Minimally Invasive Surgery. It also presents a Gaussian Process Adaptive Sampling algorithm that results in tumor localization using our probe with approximately the same accuracy as a dense raster scan while requiring at least $10x$ fewer measurements.

Overview

Robotic surgical assistants (RSAs) such as the Intuitive Surgical's da Vinci system have been shown to be effective in facilitating precise minimally invasive surgery [1, 2], by providing increased dexterity and control for the surgeon. And palpation, using the sense of touch to examine part of the body or organ, is frequently used during surgery for in-situ assessment and localization of cancerous tissue for diagnosis or tumor resection. During an open surgery, a surgeon can directly palpate tissue to identify and localize subsurface structures or tumors based on changes in tissue stiffness relative to the surrounding substrate [3].

In clinical usage, RSAs are controlled by surgeons in local teleoperation mode (master-slave with negligible time delays) and the operating surgeon depends primarily on vision for complex tasks such as tumor localization and resection. While there have been advances in providing haptic feedback for Robot-assisted minimally invasive surgery (RMIS) [4], RSAs used in clinic still largely lack haptic sensing. In spite of the increasing use of RMIS in cancer treatment [5], the lack of haptic perception as compared to open surgery can potentially increase the risk of tissue damage [6] and the likelihood of incomplete removal of cancer cells [7].

Tactile and force sensors to have the potential to provide haptic feedback in RMIS, enabling the surgeon to perform an array of survey operations such as in-situ diagnosis and localization. A recent survey of medical tactile force sensors by Konstantinova et al. [4] reports that numerous devices exist to estimate tactile information during static (point based) measurements. However, a gap exists in scanning soft tissue surfaces in a dynamic (continuous) manner. Another major limitation in the clinical use of tactile force sensing in RMIS is the need for sterilization of tools [8]. After every use, end-effectors are cleaned in an autoclave using high-pressure, high-temperature

steam. Most haptic sensors have delicate components, such as resistive strain gauges or electromagnets, which cannot withstand such a harsh sterilization process. Hence, there is a need to develop low-cost single-use tactile or force sensing devices for RMIS that operate in real-time, provide reproducible and repeatable measurements.

In addition to sensors compatible with RMIS tool-tips, automation of tumor resection also requires a high confidence estimate of both the organ geometry and the tumor boundary [9]. Uncertainty in organ geometry can result in incorrect stiffness estimates and uncertainty in the tumor (or cyst) location can result in an imprecise incision. A negative margin could result in a conservative estimate (cutting out excessive healthy tissue), while a positive margin could result in undercutting the tumor and spreading the cells.

1.1 Summary of Contributions

1. **Design of Palpation Probe:** This thesis presents a novel low-cost, disposable, haptic palpation probe to be used with the da Vinci RSA tools as discussed in Chapter 2. The probe is designed to sense relative deflection differences for localization of subcutaneous or subserous inclusions such as blood vessels or tumors. It is an indentation based device using a displacement-based contact sensing mechanism. A spherical indenter of 4.5 mm diameter allows quasi-static sliding palpation for continuous measurements.

Section 2.3 discusses the probe design details along with sliding indentation experiments on silicone-based tissue phantoms. Silicone inclusions of varying diameters ($\{1.58, 2.38, 3.175, 4.75\}$ mm) placed at varying depths ($\{1, 2, 3, 5\}$ mm) were used to evaluate probe sensitivity. For characterization of robustness to sliding surface speed, the probe was mounted on a CNC milling machine (as shown in Figure 2.3a) and was palpated across the tissue phantom in sliding at varying indentation depths ($\{1, 3, 8\}$ mm) and sliding speeds (0.5-21 mm/s). The use of the palpation probe as a tool mounted on the dVRK to perform automated sliding palpation in the silicone-based tissue phantoms is also demonstrated. Initial results suggest a potential for the clinical utility of automated sliding palpation in both supervised and semi-supervised telesurgery.

The design details are described in Chapter 2 and were published in:

• Stephen McKinley, Animesh Garg, Siddarth Sen, Rishi Kapadia, Adithyavairavan Murali, Kirk Nichols, Susan Lim, Sachin Patil, Pieter Abbeel, Allison M Okamura, and Ken Goldberg. "A disposable haptic palpation probe for locating subcutaneous blood vessels in robot-assisted minimally invasive surgery". In: *IEEE Conf. on Automation Science and Engineering (CASE)*. 2015

2. **Gaussian Process Adaptive Sampling:** This thesis also proposes an algorithm for autonomous tumor localization with palpation in RMIS for a given organ geometry. The tumor boundary localization is posed as a Bayesian optimization problem along implicit curves defined by a Gaussian Process (GP) representing estimated tissue stiffness. This approach focuses on reducing uncertainty along level sets of the surface stiffness as opposed to creating a high-certainty stiffness map for the entire search area. This approach is compared to two other palpation algorithms for mapping subsurface stiffness: one which prioritizes exploration alone, and the other which balances

exploration and exploitation of high stiffness areas, as opposed to along implicit curves.

The results evaluate the symmetric difference in the boundary estimate obtained with the ground truth in all three cases as described in Section 3.4. Simulation results suggest that as compared to EVR and UCB, ILS-UCB converges to the tumor boundary more quickly and can accommodate higher levels of measurement noise and bias (see Section 3.4). In addition to evaluation in simulation, this thesis demonstrates results for autonomous segmentation of subcutaneous tumor in soft tissue phantom with an end-effector mounted palpation sensor, presented in Chapter 2, on the da Vinci Research Kit (dVRK) [11] in Section 3.5. Experimental Results on dVRK suggest that this approach can localize the tumor boundary with approximately the same accuracy while requiring at least 10x fewer measurements than uniform raster search.

The algorithm is described in Chapter 3 and was published in:

• Animesh Garg, Siddarth Sen, Rishi Kapadia, Yiming Jen, Stephen McKinley, Lauren Miller, and Ken Goldberg. "Tumor Localization using Automated Palpation with Gaussian Process Adaptive Sampling". In: *IEEE Conf. on Automation Science and Engineering (CASE)*. 2016

1.2 Background and Related Work

Tactile force sensing is used by humans to explore, manipulate, or respond to their environment [13]. Robotic tactile sensing is applied in diverse fields including surgical devices, industrial equipment, and dexterous robotic hands [13]. In this work, we focus on the exploratory and diagnostic aspect of tactile feedback within the purview of Robot-assisted Minimally Invasive Surgery (RMIS).

Palpation sensors are a subclass of tactile and force sensors that mimic the biological sense of cutaneous touch. In RMIS, palpation sensors can estimate relative tissue stiffness and allow the surgeon to adjust force control input for safer tissue manipulation. It has been demonstrated that a RMIS tool equipped with tactile sensing under autonomous control reduces the maximum applied force to the tissue by more than 35% compared to manual palpation with the same instrument [14]. Other studies have compared human sensing with probing sensors for tumor localization and have found probing sensor arrays to be more effective in requiring lesser forces for inclusion identification [15, 16].

This work will focus on a novel palpation probe design and active search algorithms for autonomous tumor localization under observation uncertainty. The following sections detail the state-of-the-art in both of these areas.

1.2.1 Design of RMIS Palpation Probe

Modes of tactile force sensing

Tactile feedback can be obtained by using a number of transduction principles [4, 17]. The reader is referred to Girão et al. [18] and Tiwana et al. [19] for detailed surveys of existing tactile and force feedback devices in the context of robotic and biomedical applications respectively. A study

by Puangmali et al. [17] also reviews tactile sensing at the end-effectors of RSAs classified by transduction principle used in sensors.

Particularly, tactile sensing can be classified based on its underlying transduction principles: mechanical [20], piezoresistive [21, 22], capacitive [23], piezoelectric [24], strain gauge [25], optical [26], and magnetic [27]. While each of these techniques has respective advantages and limitations as listed by Tiwana et al. [19], a number of these techniques require complicated signal conditioning infrastructures, are susceptible to drift, and have a limited range of measurable forces.

Tactile force sensing in RMIS

Konstantinova et al. [4] describe of a number of RMIS tactile feedback devices and compare them based on desired features for tactile probes in RMIS such as: (a) repeatability, (b) reliability, (c) speed of sensing, (d) static versus dynamic response, (d) miniaturized form and (e) cost. Additionally, since RMIS tools are between 5 mm to 12 mm in diameter [28], hence the sensor needs to be small enough to pass through the trocar port and be placed proximal to the tool-tip. Further, strict certification requirements for medical devices warrant that these probes have high accuracy and stable response. There have been a number of efforts in probe design research to address some of these considerations [29]. Moreover, requirements for sterilization of devices are also essential considerations for the design of surgical tools [8]; heat, pressure, and humidity during treatment for tool reprocessing can destroy sensors.

Althoefer et al. [30] presented a sensor using compressed air to investigate the mechanical properties of soft tissue; maintaining constant airflow is a challenge and requires additional equipment. Murayama et al. [31] devised a sensor array for lump detection in breast cancer aimed at identifying large (> 10 mm) inclusions close to the surface (< 20 mm) but it faces limited adoption in laparoscopic procedures given its large size (45 mm in cross-section). Beccani et al. [32] developed a wireless sensor based on external static magnetic fields within a small workspace. Developments in MEMS devices have allowed a multitude of sensors to be miniaturized inexpensively. Peng et al. [33] proposed a MEMS tactile sensor which can provide fast relative elasticity measurement. Gafford et al. [34] proposed a monolithic approach to building a tri-axis force sensor for medical applications. However, none of these methods provide continuous tangential sliding surface measurements.

Liu et al. [35] used a force sensitive wheeled probe to gather a "rolling mechanical image" to observe that a continuous measurement approach is more sensitive to differences in force profiles caused by simulated tumors than single-site data acquisition. However, rolling teeth cause periodic perturbations impairing the continuous measurement. An improved design by Liu et al. [36] with a greater complexity was able to identify spherical inclusions larger than 3 mm in diameter at a depth of less than 2 mm. Non-contact sensing methods such as intraoperative MIS ultrasound probes [37] and optical coherence tomography (OCT) devices [38] have also been explored. These methods provide lower resolution compared to contact probes [4] and are limited to sensing within a comparatively low subcutaneous depth (0-2 mm).

Comparison with the proposed design

While many of the tactile and force sensors described by Konstantinova et al. [4] have a subset of desired characteristics, limitations such as repeatability, ease of manufacturing, and cost, have slowed widespread adoption in clinical settings. Many of these sensors are often operable only in a discrete mode for orthogonal point measurements and cannot survive sterilization. As concluded by [4], “A number of devices have been developed to provide accurate tactile information during static measurements from one point. However, to detect information about mechanical properties of an organ, it is required to perform dynamic tissue scans." There is a need for RMIS compatible sensors with rapid response time for stable measurements in sliding or rolling modes.

This work presents a novel low-cost, single-use RMIS tool-tip deflection measurement device for localization of subcutaneous blood vessels. This design achieves high speed sliding palpation (tested up to 21 mm/s) while maintaining high sensitivity in deflection (~50μm) and force (4mN least count). In the case of single-use devices, a design for manufacturability in a sterile environment is required but considerations for reprocessing are circumvented. The simplicity of the design presented in this work is low-cost that potentially allows utility as a single-use device. The proposed palpation probe measures displacement-based force properties of tissue using a commercially available MEMS-based Hall Effect encoder as its core sensor. Hall Effect sensors measure minute changes in electric potential produced by magnetic flux passing through a conductor; a single sensor design favorably reduces fabrication complexity [4]. We use a 4.5 mm diameter spherical probe tip as the end-effector for tangential sliding point-contact interaction analogous to human fingertip palpation. Other physical characteristics can be found in Table 2.1.

1.2.2 Tumor Search and Localization

Active Search and Mapping

Decision-theoretic approaches have been employed in best action selection problem such as active mapping problems [39]. Literature from automating grasping and grasp planning, for example, examines the problem of estimating and refining 2D and 3D estimates of objects using different sensing modalities [40, 41]. Our approach draws on prior work from adaptively estimating shapes and curves using noisy measurements. Dragiev et al. [41] represent the shape of 3D objects using Gaussian Process Implicit Surfaces (GPIS), and their algorithm explores the shape estimate by attempting grasps in areas with highest variance along the implicit surface, using information from failed grasp attempts (missing or unexpected contacts) to refine the GPIS estimate. [39] - The method uses an information gain metric based on the uncertainty of the object’s pose to determine the next best touching action and is demonstrated on a real system. In Hollinger et al. [42], coverage-based inspection paths are planned based on estimated uncertainty over a GPIS model of a ship’s hull. The method by Bjorkman et al. [40] initializes an object shape estimate using stereo vision, and calculates a GPIS representation of object geometry. The estimate is then refined by iteratively collecting haptic measurements at points along the estimated surface with the highest predicted uncertainty.

Tumor Localization with Tactile Sensing

A number of recent works focus on leveraging haptic/tactile feedback to automate mapping subsurface stiffness or material variation in soft tissue for RMIS procedures. Many approaches are concerned with creating a map of subsurface stiffness or variations in material properties using such sensors. Goldman et al. [43] recursively increase spatial resolution in areas where the measurement passes a certain threshold during stiffness mapping for haptic localization of subcutaneous tissue boundaries. Similarly, Nichols et al. [44] use elastography data from discrete measurements along a grid, train a classifier for stiffness discrimination between tumors and surrounding tissue, and perform local refinement around points identified as boundary points. Ayvali et al. [45], present an algorithm for registration of surface geometry to pre-operative data.

While many of the methods discussed above use adaptive sampling techniques, they attempt to map the complete surface. In the problem of tumor localization, a complete stiffness map is unnecessary and needs many more samples. The approach proposed in this work as described in Chapter 3 is most closely related to recent work in active level-set estimation using mobile sensors for environmental modeling [46, 47]. Hitz et al. [47] use a receding horizon path planner to reduce uncertainty specifically around a threshold value for plankton level modeling using aquatic robots. In Gotovos et al. [46], a traveling salesman algorithm is used to plan paths that sample a set of new measurement sites chosen using the same information measure. Both [46] and [47] use a sampling criterion based on the ambiguity of the function value at a particular point being above (or below) a threshold to select subsequent sampling locations. Similar to these approaches, rather than achieving low estimate error everywhere, the palpation strategy in this work is to focus on regions representing boundaries of level sets, or where a scalar function crosses a specific threshold.

However, it is worth noting that uncertainty in the stiffness map depends on the accuracy of the organ surface estimate. A few recent studies have studied tactile surface estimation [48, 49], using a high-definition multi-axis force sensor that is unavailable in the form-factor for RMIS. This work assumes that the surface estimate *a priori* is available, and hence a uniform measurement noise in the GP update can be used (see eq. (3.2)).

Chapter 2

Design of a Disposable Palpation Probe

This chapter introduces the design of a low-cost, disposable palpation probe for use with a standard da Vinci classic tool. As noted in Section 1.2.1, a palpation probe design for robot-assisted surgery has design constraints that require it to be small in profile, return observations to allow tumor localization and should operate with a functional surgical robot with possibly uncertain kinematics. This chapter describes the design constraints (Section 2.1), design principles (Section 2.2), probe characterization on a CNC vertical mill and an initial study of probe response in subcutaneous tumor localization when mounted on the end of a da Vinci Needle Driver (Section 2.3).

2.1 Palpation Probe Design

2.1.1 Design Requirements

The primary consideration for the palpation probe design in this work was to achieve high sensitivity and repeatability at a low-cost. The requirement of high sensitivity and repeatability is as a result of the probe to enable autonomous palpation and autonomous operation requires a consistent measurement model. While the need to sterilize clinical equipment entails that the probe design to be either robust to autoclave or be low-cost enough to justify disposal after single use. Additionally, requirements for compact size and resolution, as described subsequently, were also carefully considered during the design iterations.

Compact Size and Low Cost

The probe must match size constraints imposed by minimally invasive tools (diameter 5 mm to 12 mm) [28] used in laparoscopic procedures. The palpation probe was designed to mount onto the 8 mm diameter tool-tip of the da Vinci Research Kit (dVRK) Patient Side Manipulator (PSM). The current prototype adds a total length offset of 75 mm to the needle driver tool as shown in Figure 2.2. To limit costs, the probe sensing element is designed as a single-use add-on to an existing gripping tool. The gripper and data collection board may be reused.

Table 2.1: Palpation Probe Specifications

Property	Value
Probe-Tip Radius	2.25 mm
Force Resolution	4 mN
Maximum Linear Displacement	12 mm
Spring Rate	0.08 N/mm
Total Linear Offset of Device (from dVRK gripper)	75 mm
Magnetic Encoder	NSE5310
Pole Pair Length	2 mm
Number of Pole Pairs	6

Resolution in Deflection

Palpation measurements are improved by matching the impedance of test probe to sampled tissue. If the sensor is excessively stiff there would not be a measurable deflection in the probe tip to register an inclusion. If the sensor is too pliable tissue inclusions would not be registered as probe tip deflections. While searching for subcutaneous inclusions, it is essential to indent appreciably within the tissue to observe a deflection in the probe, as demonstrated later in the experiments (see Figure 2.5(c)). The total displacement of the device was designed to be 10 mm with replaceable springs to allow for operation over tissues of different stiffness values.

2.1.2 Principle of Operation

The probe uses Hall Effect sensing to compare displacement from the palpation probe to a known deflection value taken from a relative sample. The probe tip displacement (δ_p) relative to the body of the device is measured with an incremental magnetic encoder and can be linearly related to a tissue reaction force (F) using Hooke's Law ($F = k\delta_p$). The spring constant is known apriori and in this case chosen to be $k = 0.08\,\mathrm{N/mm}$.

For this device the indentation depth d_i can be calculated from the relative positions of the

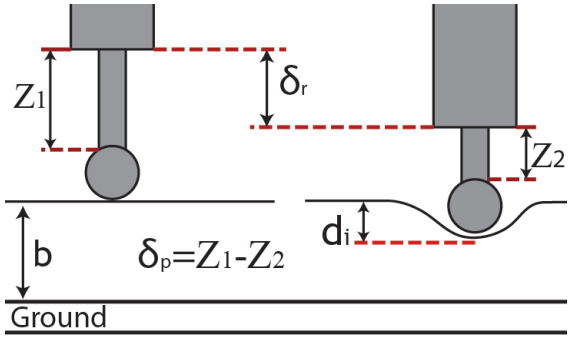

Figure 2.1: A schematic illustrating the indentation process as well as the parameters which define the relationship between indentation depth and probe-tip deflection as described in Section 2.1.2.

device (position of the robot arm), end effector (displacement of probe tip), and the baseline height (b) as (see Figure 2.1):

$$\begin{aligned} \delta_p &= Z_1 - Z_2 \\ d_i &= \delta_r - (\delta_p - b) \end{aligned} \tag{2.1}$$

where d_i is the depth of indentation, δ_p is the probe-tip displacement, δ_r is the displacement of the palpation probe body along the contact normal with respect to the datum, and b is the baseline height of the sample.

2.2 System Design

2.2.1 Sensing

Deflection of the probe tip was measured with an NSE5310 Austria Microsystems incremental position sensor. Magnetic Hall Effect sensors (such as the NSE5310) do not require direct contact with the sensed element which minimizes friction between the probe tip and the body of the device. The probe tip and axisymmetric magnet column were free to rotate with respect to the shaft of the da Vinci robot allowing the palpation probe to slide and rotate while in contact with surfaces. The NSE5310 magnetic encoder was mounted on the reverse of the electronics board and was located 0.125 mm from a central column of magnets which followed the movement of a 2.25 mm radius spherical indenter. Neodymium disc magnets (of 2 mm diameter and 2 mm pole pair length) were installed within the sense column with an inter-magnet air-gap of 2 mm. There were 4 magnets within the central column yielding a theoretical total displacement of 16 mm. Hard-stops were placed on the device to limit total displacement to 12 mm. The central column was made from magnetically permeable 316 Stainless Steel with a wall thickness of 0.23 mm and slid co-axially within 316 Stainless Steel bushings. Magnetic permeability is critical for allowing lines of flux to pass through the magnetic column to the NSE5310 Hall Effect sensors. An internal view of the mechanical components can be seen in Figure 2.2a.

2.2.2 Electronics Design

To reduce size and cost, only components critical to sensing and voltage stability were included onboard the sensor. The power supply for the NSE5310 encoder was buffered and isolated using low-pass capacitors. A power indication LED and a current limiting 470 Ω resistor were included for debugging. The total footprint of the electronics board is less than 15 mm per edge as illustrated in Figure 2.2b.

2.2.3 Signal Processing and Data Linearization

An Arduino Mega microprocessor was used for signal processing, data transmission, and interfacing with the dVRK. The NSE5310 encoder transmits 14-bit position measurements to the Arduino

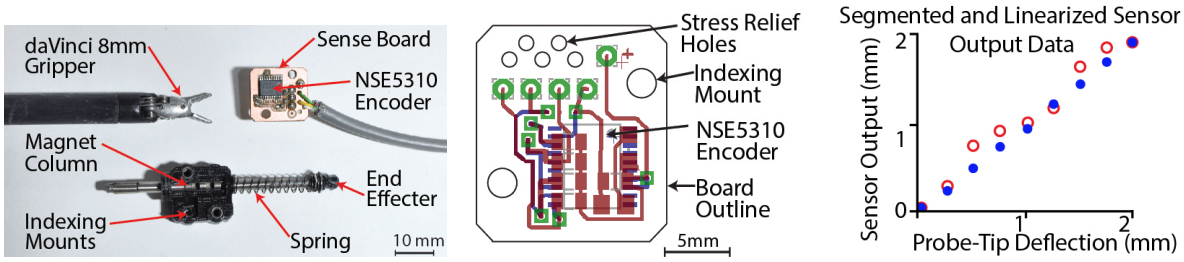

(a) (b) (c)

Figure 2.2: An exploded view of palpation probe components. (a) Internal components of the probe with 8 mm da Vinci needle driver for comparison. The mounting bracket for the sensor is not shown. (b)Two layer printed circuit board design of the Sense Board showing surface mount components on top layer in red and bottom layer in blue. Connectors have been omitted from the design in the interest of minimizing size. (c) Linearization of output: Raw output of the sensor with respect to actual probe-tip position shown as red circles, cleaned data with non-linearities removed in real time signal processing as described in Section 2.2.3 are shown in solid blue.

via I2C at a rate of 300Hz. A 50 sample sliding average low-pass filter was used to condition the raw encoder measurements.

The absolute position between magnet pole pairs was calculated as a 14-bit integer in software by comparing any two consecutive readings and shifting the most significant bit up or down by one if the differences between consecutive readings were greater or less than a shifting threshold of 4000 or -4000 respectively. The shifting threshold was chosen to be greater than 6 standard deviations of the noise away from the maximum sensor value of 4096 (sensor noise is addressed below).

Sensor output was recorded at known probe-tip indentation depths by mounting the sensor in a computer numerical controlled (CNC) Bridgeport vertical milling machine, as shown in Figure 2.3a, equipped with a digital readout and accurate to 0.01 mm. For every probe tip position, $10,000$ samples were collected and averaged. These data points revealed a non-linearity between probe output and CNC measured compression as illustrated in Figure 2.2c. Transitional air gaps between magnetic pole-pairs, spaced alternately every 2 mm as seen in the *Magnet Column* in Figure 2.2a, create non-linearities in magnetic flux along the axis of travel. A six-degree polynomial was fit to the 4 mm repeating segment of data used by the microprocessor to scale probe-tip indentation depth to a linear output as shown in Figure 2.2c.

2.2.4 Cost Estimates

The total cost for the electronics on the disposable printed circuit board was less than $7.00 at the single-unit prototype scale. The structural hardware can be injection molded or made from simple tubular components and modular springs and cost less than $2.00. The magnets in the probe cost approximately $0.01 each.

2.3 Experimental evaluation of Palpation Probe

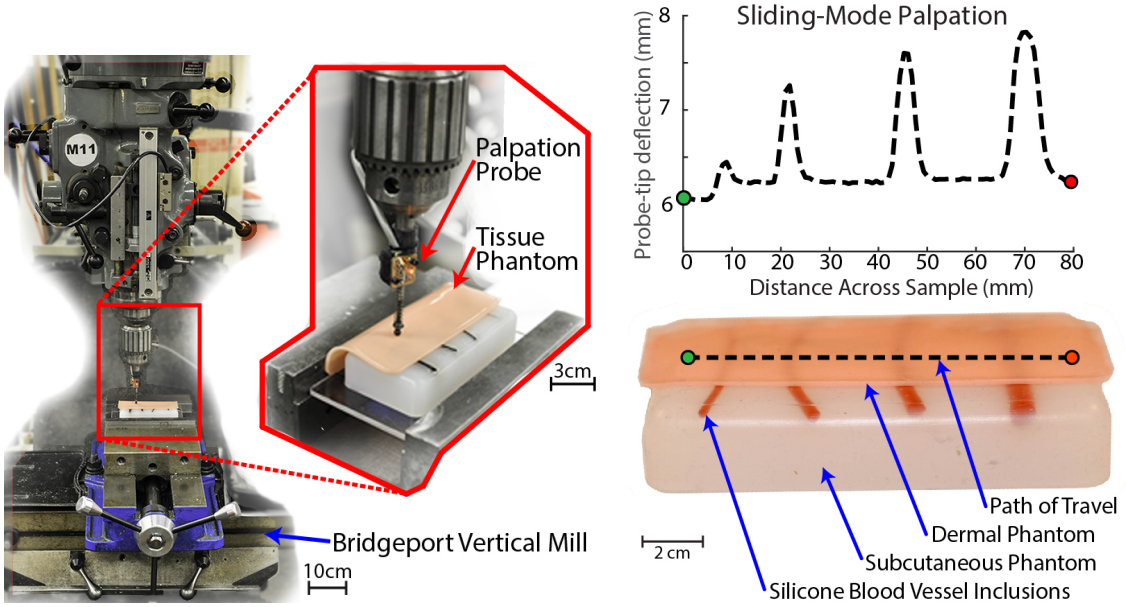

(a) Probe characterization on a CNC Vertical Mill (b) Probe Output for a tissue phantom

Figure 2.3: (a) Probe characterization on a Bridgeport CNC (XY-Axis) Vertical Mill. The vertical axis movement (δ_r in Equation 2.1) was measured by a digital encoder (accurate to 0.01 mm). For every setting of indentation depth, the vertical position was held constant as the tissue phantom was moved along a linear path across the subcutaneous vessels. (b) A silicone tissue phantom is shown with blood vessel inclusions and overlaid dermal phantom. sliding palpation from starting point (green circle) to end point (red circle) over 80 mm of travel reveals the presence of subcutaneous blood-vessel inclusions as observed from the probe-tip deflection in the graph above. Depth of indentation was held constant at 8 mm, sliding speed was 1 mm/s, and skin thickness was 1 mm.

2.3.1 Tissue Phantom with Linear Vessels

A tissue phantom comprising a cutaneous layer with subcutaneous inclusions was created for testing and characterization of the stiffness probe, as shown in Figure 2.3b. Silicone Rubber *Ecoflex 00-30* (*Smooth-On*) was cast in a 1A:1B ratio into a 100 mm long, 50 mm wide, 20 mm thick mold CNC machined from a block of *Delrin* to create a subcutaneous tissue matrix. Linear cylindrical inclusions of Silicone Rubber (thickness $\{1.58, 2.38, 3.175, 4.75\}$ mm; Shore hardness of 70A) were arranged in the bottom of the mold prior to casting to serve as subcutaneous blood vessel phantoms. After setting, the subcutaneous phantom was unmolded and inverted. A cutaneous phantom was created using a slightly stiffer (shore hardness 2A) *DragonSkin 10 Medium* Silicone Rubber (*Smooth-On*) in a 1A:1B ratio. Opaque pigmentation was achieved using a 0.5% by volume addition of Oil Pigment (Winton Oil Colour, Flesh Tint). The pigmented dermal layer was cast at various thicknesses ($\{1, 2, 3, 5\}$ mm) in molds milled from *Delrin* (with width of 60 mm and length of 100 mm). Upon solidification,the dermal phantom was overlaid on the subcutaneous phantom (as shown in Figures 2.6b) to create the tissue phantom setup.

2.3.2 Calibration using CNC Tool

The probe was affixed to a *Bridgeport* CNC vertical mill (with digital encoders accurate to 0.01 mm) for sensor calibration similar to the linearization procedure in Section 2.2.3. The tissue phantom was mounted securely to an acrylic plate affixed in a vise. The vertical position of the sensor was held constant at an initial probe deflection of 2 mm while the tissue phantom along with a cutaneous layer (lubricated by petroleum jelly) was moved beneath the sensor at a feed rate of 1 mm/s. Each trial was conducted across the same line running transverse to the veins embedded in the tissue phantom as shown in Figure 2.3b. The standard error across 10 trials, quantified by a normalized root mean square difference, was found to be $0.931\,\mu m$.

Baseline sensor noise data ($> 10,000$ samples) were collected with no signal processing; the standard deviation of the noise was found to be $12.9\,\mu$m. A measured value $52\,\mu$m (~4σ) above baseline can be considered statistically dissimilar from noise; and using $F = k\delta_p$, we can get a minimum palpation probe sensitivity of 4 mN.

2.3.3 Probe Characterization using CNC Tool

A surface profile was constructed by interpolating the δ_r position of probed surface contact points spaced at 10 mm intervals along areas of interest. A surface contact point is described as the first time the probe registers a non-trivial measurement upon touching the surface; quantitatively defined as the δ_r position of the sensor after statistically significant deflection ($4\sigma \approx 52\ \mu$m) is observed at the probe-tip (δ_b). This profile accounts for physical irregularities in the sample surface shape and is used to account for surface offset represented by b in Equation 2.1.

Figure 2.3b shows the probe-tip deflection (δ_p) using a sliding measurement across the silicone tissue phantom with blood vessel phantoms and overlaid dermal phantom. The probe was slid across the surface from the starting point (green circle) to end point (red circle) over 80 mm of displacement. Parameters used in this trial were: indentation depth (δ_r) of 8 mm, sliding speed of 1 mm/s, and a skin thickness of 1 mm.

Deflection Response Characterization

Localization of a subcutaneous blood vessel (or tumor) depends on several parameters such as the *indentation depth*, *depth of the vessel* below the surface, and *speed of probe sliding*. Characterization of the probe behavior is essential to analyze the deflection response for different parameter settings.

Probe response was tested by varying each of these parameters for a fixed value of the other two as shown in the series of graphs in Figure 2.4. Each graph in the figure shows the variation in probe-tip deflection for different indentation depths (1 mm, 3 mm, 8 mm) at a fixed skin thickness and a constant sliding speed of 1 mm/s. The different graphs show the variation for different skin thicknesses (1 mm, 2 mm, 3 mm, 5 mm).

Similarly, fixing the indentation depth at 8 mm and skin thickness at 1 mm, we varied the sliding speed to four different settings, ($\{0.5, 1, 6.3, 21\}$ mm/s) and observed the probing response

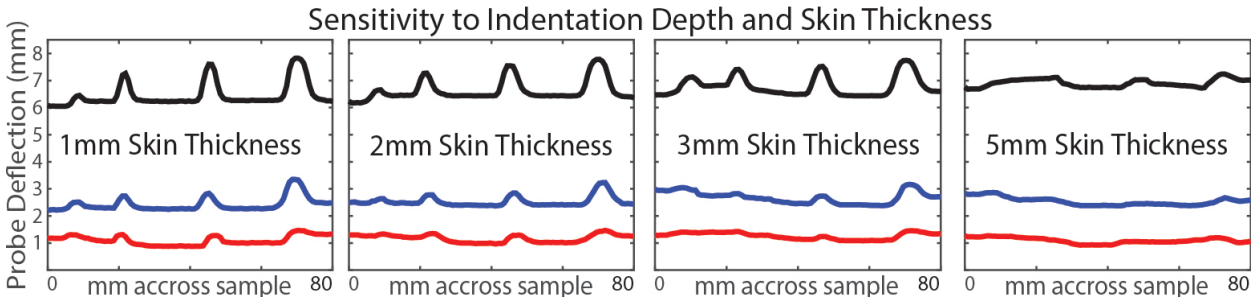

Figure 2.4: Increasing Skin thickness decreases palpation probe sensitivity, while increasing penetration depth increases probe sensitivity to buried blood-vessel phantoms. Displacement of the probe-tip during sliding palpation plotted at 1 mm/s surface speed; indentation depth (δ_r) of 1 mm shown in red, 3 mm shown in blue, and 8 mm shown in black.

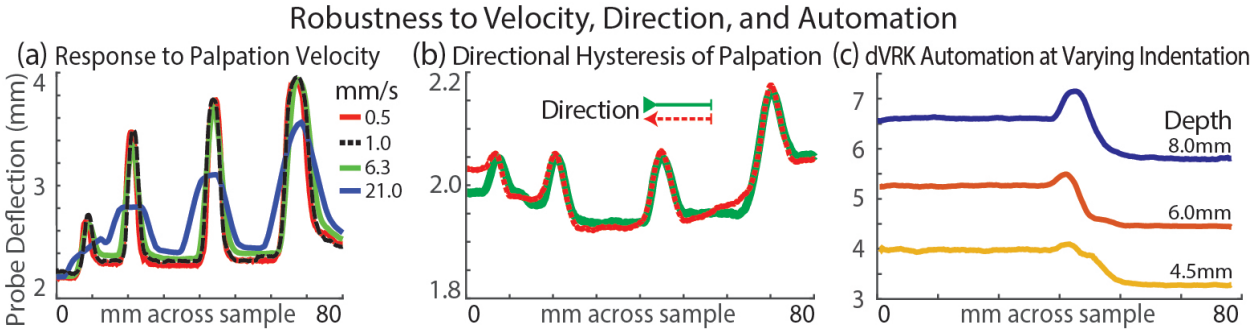

Figure 2.5: Sensor response was tested with respect to varying speed and direction on CNC vertical mill, and automation by the dVRK. (a) robustness to sliding speed was tested at four surface feed-rates; 0.5 mm/s is shown in red, 1 mm/s is shown in black, 6.3 mm/s is shown in green, and 21 mm/s is shown in blue. Probe indentation depth was held constant at 8 mm; skin thickness is 1 mm. (b) Hysteresis of sliding palpation collected continuously in opposite directions without lifting the probe. The maximum maximum difference between data observed are within 4σ of noise levels, indicating very low hysteresis. Motion in the positive x-direction is shown in red; negative x-direction palpation is shown in green. This data was collected using a 1 mm skin thickness and 2 mm indentation at 1 mm/s sliding speed. (c) Deflection of palpation probe at three different indentation depths with an automated routine on the dVRK.

as shown in Figure 2.5(a). The probe was used to acquire deflection measurements along the same raster line in a forward and a backward pass. The results from this hysteresis analysis are shown in Figure 2.5(b); the maximum difference between the directional data was not statistically significant ($\geq 10\times$ larger than 4σ of Gaussian noise).

2.3.4 Autonomous Palpation with dVRK

The palpation probe was mounted on the end of an 8 mm da Vinci Needle Driver as shown in Figures 2.6b and 2.6a, extending the tool tip by 75 mm. Figure 2.5(c) shows the deflection response obtained for three indentation depths ({4, 6, and 8} mm) at 2 mm/s in single-sweep automated sliding palpation.

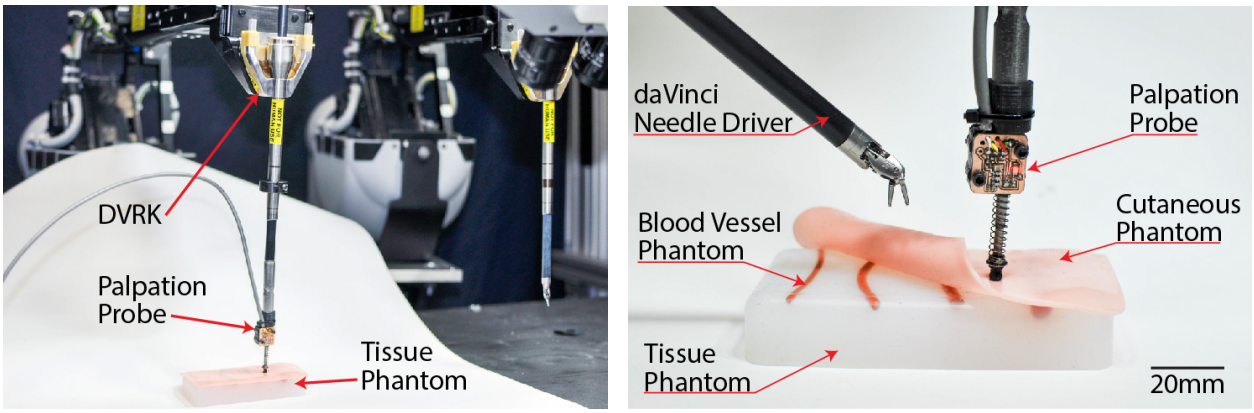

(a) Overall Setup (b) Probe Output for a tissue phantom

Figure 2.6: (a) A disposable palpation probe mounted on the tip of an 8 mm diameter dVRK needle driver tool. (b) It is also shown alongside a regular 8 mm diameter da Vinci tool and a with a tissue phantom with subcutaneous vessels. This device is a low-cost extension to an existing da Vinci tool for acquiring tactile information from surface probing in robot-assisted minimally invasive surgery. The presented design of the palpation probe can be automated to search for blood vessel phantoms with the da Vinci Research Kit Patient Side Manipulator.

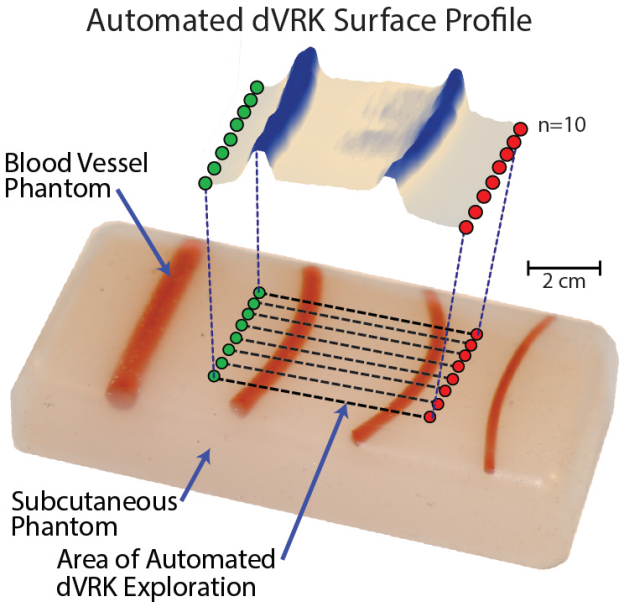

Figure 2.7: An estimate of subcutaneous blood vessels generated by as raster scan on the region of interest. Delaunay surface interpolation was used to create a continuous estimate from raster samples. Start and end points for each linear segment are shown overlaid above a tissue phantom as green and red circles respectively with indicative raster scan paths (shown as black dashed lines).

An autonomous palpation routine was created for the dVRK accounting for the linear offset along the insertion direction as shown in Figure 2.7: a plane representing the surface of the tissue phantom was created by recording the pose of the dVRK at the four corner points defined by point-contact of the palpation probe ($\geq 50\,\mu$m indentation). This plane (45 mm $\times$ 25 mm) was segmented into 10 linear palpation sub-routines transversely crossing two subcutaneous blood vessel phantoms. The dVRK returned the palpation probe-tip to a home position 2cm above the area of interest between each linear segment. Continuous tangential palpation at 2 mm/s with an indentation depth of 8 mm was used to search within the area of interest on the tissue phantom. The blood vessel silicone phantoms used for these trials were 2.5 mm and 3.5 mm in diameter embedded subcutaneously beneath a layer of 1 mm thick dermal phantom. An estimate of the location of subcutaneous vessels generated by Delaunay interpolation of a raster scanning pattern is illustrated in Fig. 2.7. Start and end points of the raster path are shown overlaid above a tissue phantom as green and red circles respectively.

2.4 Discussion of Results

Preliminary characterization results from the palpation probe demonstrate the ability to identify and localize a subcutaneous blood vessel. As we observe in Figure 2.3b, as the size of the underlying vessel increases the sensor deflection also increases. In all cases, the deflection obtained is significantly above the noise ($\geq 10\times$ larger than 4σ of Gaussian noise). Increasing depth of the inclusion decreases the signal-to-noise ratio from 40:1 at 1 mm skin thickness to ~4:1 at 5 mm skin thickness for a vessel of diameter 4.75 mm. Signal-to-noise ratio amplifies approximately linearly with increase in indentation depth as observed in Figure 2.4. A discernible peak is obtained even in the raw data without signal conditioning for a subcutaneous vessel of 2.25 mm diameter under a 5 mm skin with an 8 mm indentation depth. As we increase the sliding speed of the probe on the phantom surface, we observe a small decrease in signal-to-noise ratios as shown in Figure 2.5(a). However, even the speed of 21 mm/s, which is comparatively high in the context of RMIS, we obtain statistically significant deflections for all 4 subcutaneous vessels.

Repeatability of measurements is required of RMIS probes which are supported by measurements obtained from forward and backward runs of the probe along the same raster line. These measurements are within acceptable noise levels of $50\,\mu\text{m}(\approx 4\sigma)$ as shown in Figure 2.5(b).

Experiments with autonomous palpation routines on dVRK corroborate the findings from probe characterization on CNC machine tool. In spite of the millimeter level positioning inaccuracies in the dVRK, Figure 2.5(c) shows a high gain in signal with an increase in indentation depth with constant skin thickness and sliding speed. Further, the raster scan results from Figure 2.7 demonstrate that this method can be used to search and localize a subcutaneous inclusion in a large surface area and can be automated for use by RMIS devices.

Chapter 3

Guassian Process Adaptive Sampling

This chapter introduces the design of a low-cost, disposable palpation probe for use with a standard da Vinci classic tool. As noted in Section 1.2.1, a palpation probe design for robot-assisted surgery has design constraints that require it to be small in profile, return observations to allow tumor localization and should operate with a functional surgical robot with possibly uncertain kinematics. This chapter describes the design constraints (Section 2.1), design principles (Section 2.2), probe characterization on a CNC vertical mill and an initial study of probe response in subcutaneous tumor localization when mounted on the end of a da Vinci Needle Driver (Section 2.3).

This chapter details active tumor localization with Gaussian process adaptive sampling. Prior art in active search, as described in Section 1.2.2, has attempted similar problems in localization. However, majority of the focus has been on complete surface mapping which often results in minimizing estimate variance everywhere. This chapter highlights that the search can be focused only on the tumor boundaries which can result in high-quality estimates in 10x fewer samples. This chapter formalizes the tumor localization problem, introduces Gaussian Process adaptive sampling with an implicit level set upper confidence bound (ILS-UCB). Furthermore, the proposed method is compared in the simulation with other methods to provide intuition and is compared to physical experiments with raster search methods using a da Vinci system (Section 3.5).

3.1 Problem Statement

This chapter looks at the problem of localizing the boundary of a subcutaneous tumor using a palpation probe that provides a measure of effective surface stiffness.

Assumptions. We assume a single, solid, connected 3D tumor is embedded in a volume of tissue. We assume the tumor is within depth d from the surface, resulting in measurable stiffness differences, and that the difference in stiffness measured at the surface due to the embedded tumor is at least Δk. We assume that we have access to the surface of the tissue for probing, the surface geometry is known, and the boundary of the tumor projected on the surface is smooth with an upper bound on the local curvature (κ).

Expected Output. The goal is to estimate the nonparametric curve $\mathcal{C}$ representing the projection of the subcutaneous tumor(s) $\mathcal{T}$ on the soft tissue surface. The curve is defined by level sets of the stiffness $\mathcal{S}(x)$ over the surface parameterized by $x \in \mathbb{R}^2$, measured using the palpation probe. Our algorithm produces a sequence of locations on the surface for palpation.

Evaluation. In our simulation experiments, we assume we have access to the ground truth of the inclusion boundary, $\mathcal{C}_{GT}$. We evaluate the proposed method and compare to other sampling approaches by comparing the symmetric difference between ground truth $\mathcal{C}_{GT}$ and the algorithm estimate $\mathcal{C}$. Note that we penalize both under and overestimation equally.

3.2 Gaussian Process Adaptive Sampling

Algorithm overview

The stiffness map estimate $\mathcal{S}(x)$, represented as a Gaussian process (GP), is initialized with measurements collected at randomly selected locations. Based on the current estimate and uncertainty, measurement locations are iteratively selected according to sampling criterion, defined in Section 3.3, to refine the estimate. Measurements are taken and appended to the set of data used to retrain the Gaussian Process. The updated estimate is then used to select new locations to probe.

Gaussian Process Model

GPs extend multivariate Gaussian distributions to infinite dimensions [50]. GPs are often used to estimate and model continuous spatial data. GP models provide a smooth estimate everywhere, even given sparse sets of training data, allow multi-modal sensor fusion, and provide a statistical representation of the estimate useful for active refinement using Bayesian optimization methods. We use a GP to represent the stiffness $\mathcal{S}(x)$ and associated uncertainty from the observed palpation measurements.

The input data for a GP is a set of training data D with observations Y taken at states X, or $D = \{X,Y\} = \{(x_1,y_1),...(x_n,y_n)\}$ for a set of n training samples. The GP model assumes a function f is a noisy spatial process $y_i = f(x_i) + \delta$, where $x \in \mathbb{R}^2$, $\delta \sim \mathcal{N}(0,\sigma)$ is additive zero-mean Gaussian measurement noise. Given training data D, the posterior distribution for the function $f(\cdot)$ at new points x^+ is Gaussian with mean μ_{x^+} and variance $\sigma^2_{x^+}$, i.e. $p(f(x^+)|x^+,X,Y) = \mathcal{N}(f(x^+);\mu_{x^+},\sigma^2_{x^+})$, where

$$\mu_{x^+} = k_+^T (K + \sigma_n^2 I)^{-1} Y, \tag{3.1}$$

$$\sigma^2_{x^+} = k(x^+,x^+) - k(x^+,X)^T (K + \sigma_n^2 I)^{-1} k(x^+,X) \tag{3.2}$$

Here $k(x^+,X)$ is the $n \times 1$ vector of covariances between x^+ and the n training inputs X, K is the covariance matrix of the inputs X, and σ_n^2 is the noise variance of the additive measurement noise $\delta(.)$. The covariance function (or kernel) K determines the correlation between input locations x_i. We use the squared exponential kernel [50] for the experiments in this chapter because they produce very sooomth output, but other kernels such as Matern and Periodic ones may also be used based on the domain.

Tumor Boundaries as Implicit Surfaces

The stiffness $\mathcal{S}(x)$ can be used to define the tumor boundary contour $\mathcal{C}$. Implicit curves are defined by the set of points for which an implicit function—a scalar-valued function defined over $\mathbb{R}^2$—takes on a particular value [51–53]. We define the tumor boundary ($\mathcal{C}$) as an implicit curve based on the GP representing the stiffness $\mathcal{S}(x)$, i.e. as the α-level set for the stiffness $\mathcal{S}(x)$, such that:

$$\mathcal{S}(x)\begin{cases} = \alpha, & x \text{ on } \mathcal{C} \\ > \alpha, & x \text{ inside } \mathcal{C} \\ < \alpha, & x \text{ outside } \mathcal{C}. \end{cases} \tag{3.3}$$

Since $S(x)$ is an estimate with associated uncertainty, we define the implicit curve using the GP mean and choose α based on maximum and minimum deflection measurements observed, representing likely tumor boundaries. This relaxes the need to define precise expected stiffness measurements prior to probing.

3.3 Palpation Algorithms

As described in Section 3.2, the GP representation of the stiffness $\mathcal{S}(x)$ can be leveraged by an algorithm to balance exploration and exploitation for tumor localization. We introduce three palpation algorithms that are evaluated in Section 3.4. All three iteratively select measurements by optimizing a *sampling criterion* $\mathcal{A}(\mu_{t-1}(x), \sigma_{t-1}(x))$, parametrized by the sufficient statistics of the GP estimate, the mean $\mu(x)$ and variance $\sigma(x)$.

Sampling criterion are often referred to as *acquisition functions* in GP optimization. In all 3 of these cases, we select sampling locations that maximize the criterion over the search space $\mathcal{X}$. Because the variance depends only on the locations of samples (see eq. (3.2)), not the measurements, one can select sets of sample points that take into account local variance decrease following measurements, prior to taking them. Following [46], we select a set of samples during each iteration of the algorithm using the estimated mean and the known variance from the prior iterations and solve a traveling salesmen problem approximately to plan paths between the selected measurement locations.

1. Expected Variance Reduction (EVR)

The EVR algorithm is a purely *exploratory* approach, selecting sampling points where the variance of the Gaussian process estimate is highest: i.e.

$$x_t = \arg\max_{x \in \mathcal{X}} \quad \sigma_{(t-1)}(x).$$

2. Upper Confidence Bound (UCB)

The UCB palpation algorithm balances exploration, i.e. prioritizing areas with high uncertainty (high GP variance σ) and exploitation i.e. areas where the expected stiffness is high (high GP

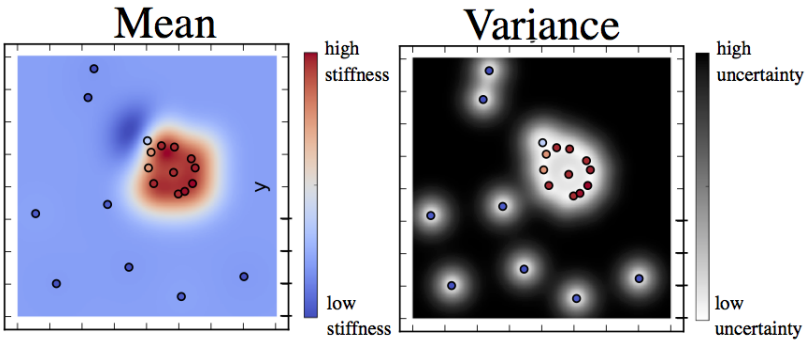

(a) GP Mean and Variance Estimate

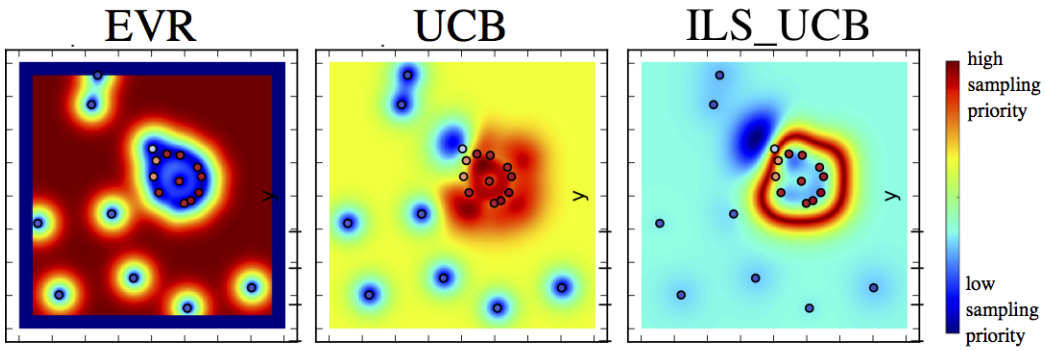

(b) Three different Palpation Algorithms

Figure 3.1: (a) Mean and variance of a circular tumor for Gaussian process estimate after 2 iterations of batch size 10 in simulation. (b) Different palpation algorithms evaluated for the Gaussian Process estimate (a). EVR prioritizes exploration in unsampled regions, UCB prioritizes exploitation of the maximum stiffness areas and uncertainty, and ILS-UCB balances sampling near level sets between the max and minimum values, and uncertainty.

mean μ):

$$x_t = \arg\max_{x \in \mathcal{X}} \quad \gamma * \mu_{t-1}(x) + (1-\gamma)\sigma_{t-1}(x).$$

Prioritizing high stiffness areas guides sampling toward regions that are likely to be tumor vs. surrounding tissue, and prioritizing high variance regions prioritizes sampling where the confidence bound is very large (there is high uncertainty in the stiffness estimate).

3. Implicit Level Set Upper Confidence Bound (ILS-UCB)

The ILS-UCB algorithm also trades off between exploration and exploitation. This algorithm prioritizes searching the expected tumor boundary, conditional on estimate uncertainty, and does not seek to precisely learn a stiffness map of the entire workspace. Intuitively, by reducing the estimation space to specifically localize the tumor boundary, we can reduce the total number of measurements–and consequently the time–required to achieve an estimate of the boundary.

Hence, rather than prioritizing the both high variance and high mean like UCB, ILS-UCB prioritizes sampling in areas near a level set of the mean represented by the Gaussian process implicit surface, i.e. to minimize the implicit potential defined by $\mu_{t-1}(x) - h_{t-1}$, and where the confidence interval is large:

$$x_t = \arg\max_{x \in \mathcal{X}} \quad (1-\gamma)\sigma_{t-1}(x) - \gamma * |\mu_{t-1}(x) - h_{t-1}| .$$

The level set h_{t-1} is not assumed *a priori*, but is a percentage α of the current estimated mean: $h_{t-1} = \alpha\,(max\mu_{t-1}(x) - min\mu_{t-1}(x))$. Note that the second term in the equation above is negative, as we are trying to sample in locations where the distance to the level set is minimized.

3.4 Simulation Experiments

We compare the three palpation algorithms described in Section 3.3 in simulation for estimation of two phantoms with known tumor geometry: 1) a circular disk (area $1.23\,cm^2$) and 2) a horseshoe (area $1.26\,cm^2$). The search space is a 2.5×5 cm region. For the selection of sampling points, the search area was discretized into a 200×200 grid (40,000 points), and γ for the UCB and ILS-UCB algorithms was chosen to be 0.5, which empirically balanced exploitation and exploration well for this application. In the simulations experiments, we use 5 initial measurements and a 50% level set (α) of the stiffness map as the tumor boundary which is indicated as the tumor boundary in Figure 3.2. We use Python package GPy [54] to implement Gaussian process regression.

We evaluate the performance of all three algorithms varying two possible noise sources: additive measurement noise (σ), and systematic measurement bias (β). The latter arises when, for example, unmodeled deviations in the palpation surface lead to systematic error in the stiffness measurements due to non-constant probe indentation.

Measurements are simulated using a *sigmoidal* model, which approximates the probe measurements made using our a customized sensor, *PALP* [10],

$$Y(x) = Y_{min} + \frac{Y_{max} - Y_{min}}{1 + \mathrm{e}^{-k(x-\mathcal{C})}} + \delta + \beta x_1 (Y_{max} - Y_{min}), \tag{3.4}$$

where k represents the slope, Y_{min} and Y_{max} the maximum and minimum measurements, and $(x - \mathcal{C})$ is the distance between points x and the closest point on the tumor boundary. δ is additive measurement noise ($\delta \sim \mathcal{N}(0, \sigma)$), and we use a linear measurement bias $\beta x_1 (Y_{max} - Y_{min})$ that increases from 0 along one dimension x_1 (vertical dimension in Figure 3.2), proportional to a bias constant β.

Table 3.1 shows the final boundary error for each palpation of the three algorithms and two phantoms. Each value is the symmetric difference error between the estimated boundary (α is the 50% level set of the mean) and the ground truth tumor boundary, as a percentage of the search area averaged over five trials. Measurement noise (σ) is shown as a percentage of the difference between the simulated measurement maximum and minimum. Measurement bias constant β is shown as a percentage of the difference between the measurement maximum and minimum.

Table 3.1: Simulation: Symmetric difference of boundary estimate from the Ground Truth with varying levels of measurement noise and bias in the measurement function (see eq(3.4)) for each of the three probing algorithms. We use two tumor models, a circular disk shaped tumor (#1) and a horse-shoe shaped tumor (#2). Error is reported as a percentage of the search space area after 10 iterations (with a batch size of 10, i.e. 100 measurements), averaged over five trials. Using the ILS-UCB palpation algorithm outperforms other algorithm in most cases and achieves up to *10x* reduction in error.

Variance (σ)	Tumor#1 Circular Disk			Tumor#2 Horse-Shoe		
	EVR	UCB	ILS-UCB	EVR	UCB	ILS-UCB
1 %	0.840	0.567	**0.056**	1.467	1.001	**0.175**
5 %	0.807	0.672	**0.177**	1.525	1.256	**0.373**
10 %	1.189	0.951	**0.393**	2.155	2.135	**0.749**
25 %	2.610	2.870	**1.314**	3.987	5.116	**2.210**

Bias (β)	Tumor#1 Circular Disk			Tumor#2 Horse-Shoe		
	EVR	UCB	ILS-UCB	EVR	UCB	ILS-UCB
1%	0.759	0.573	**0.060**	1.255	1.093	**0.141**
5%	0.667	0.818	**0.267**	1.460	1.186	**0.305**
10%	5.064	5.085	**3.906**	4.212	4.881	**3.234**
100%	11.084	10.818	**9.810**	**10.084**	10.085	10.091

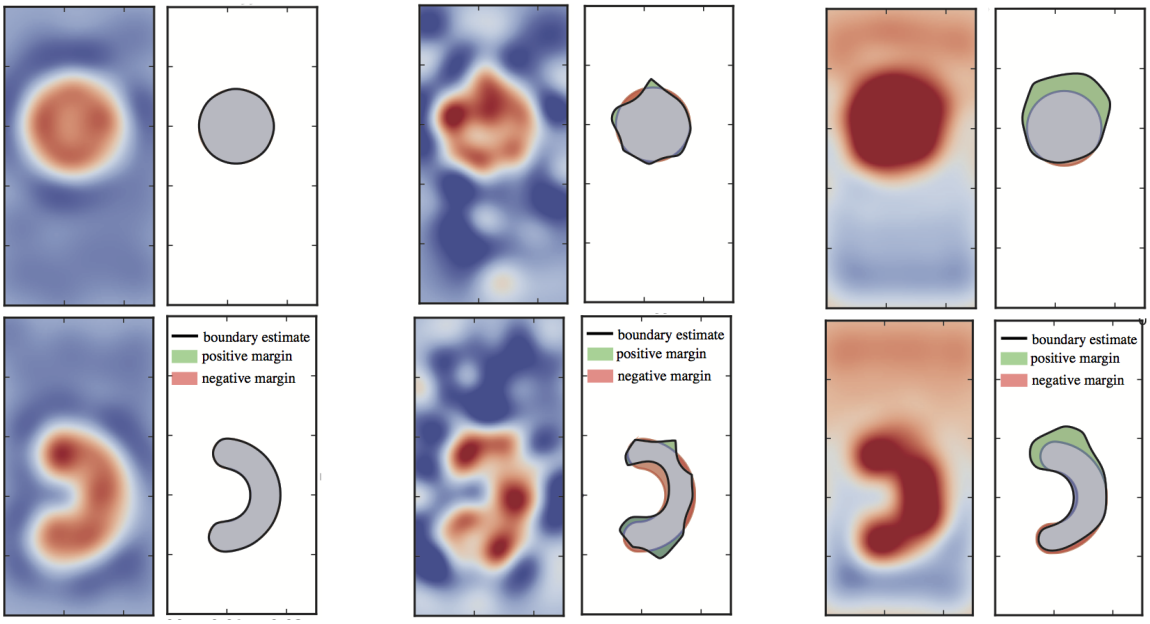

(a) noise=1%, bias=0 (b) noise=25%, bias=0 (c) noise=1%, bias=100

Figure 3.2: Estimated stiffness maps and boundary estimates for simulated experiments after 10 iterations (of batch size 10, i.e. 100 measurements) using the ILS-UCB algorithm, for different noise levels and measurement bias. Regions in blue denote surrounding tissue with lower stiffness and regions in red denote higher stiffness.

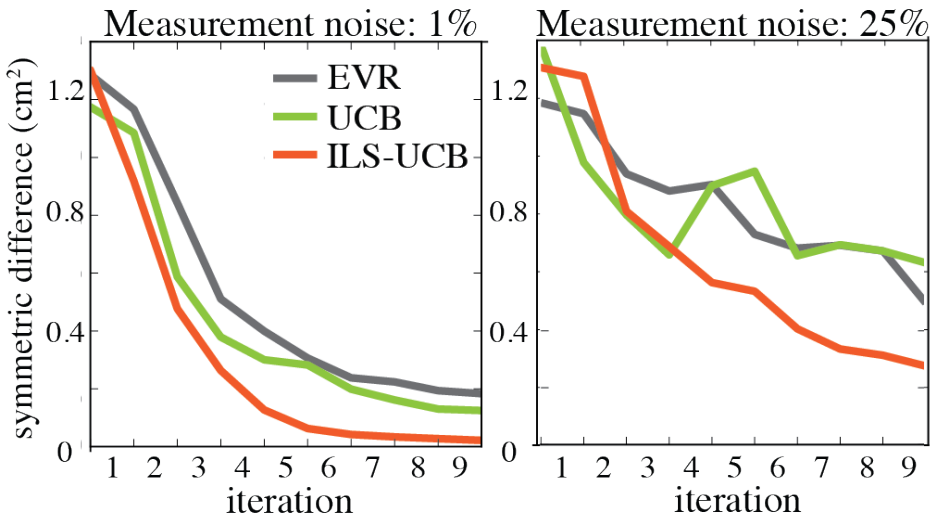

Figure 3.3: Simulation Experiments: Convergence of the symmetric difference error (as % of search space area) for palpation algorithms as a function of iteration for two different levels of measurement noise, using a horseshoe shaped tumor in simulation. As the noise increases, there is randomized exploration which results in non-smooth convergence curves in the right graph.

Figure 3.2 shows three cases of varying noise and bias levels with corresponding stiffness mean and estimated boundary for both tumors. Figure 3.3 shows the error for the horseshoe tumor (tumor 2) as a function of iterations, at two measurement noise values, for all three algorithms. Performance for all three algorithms degrades with increasing noise and measurement bias, and all three algorithms have a similarly high error for the highest noise and bias cases.; the final error is up to 10% smaller, however, using the ILS-UCB algorithm.

3.5 Physical Experiments

In this section, we evaluate the performance of the ILS-UCB algorithm, which outperformed the alternative algorithms in simulation, for tumor localization on a physical phantom using the dVRK robot. We compare the ILS-UCB algorithm to a dense raster scanning strategy, evaluating the total number of measurements made, time, and error between the estimated boundary and the Ground Truth.

dVRK: Hardware and Software

We use the Intuitive Surgical da Vinci Research Kit (dVRK) surgical robot assistant with a setup similar to described in [55, 56]. We interface with the dVRK using open-source electronics and software developed by WPI and Johns Hopkins University [57]. The software system is integrated with ROS and allows direct robot pose control. We use the customized sensor, *PALP*, presented in Chapter 2. *PALP* is a low-cost, disposable sensor that mounts on a DVRK classic tool-tip. The PALP probe uses a displacement-based contact sensing mechanism as discussed in Section 2.1.

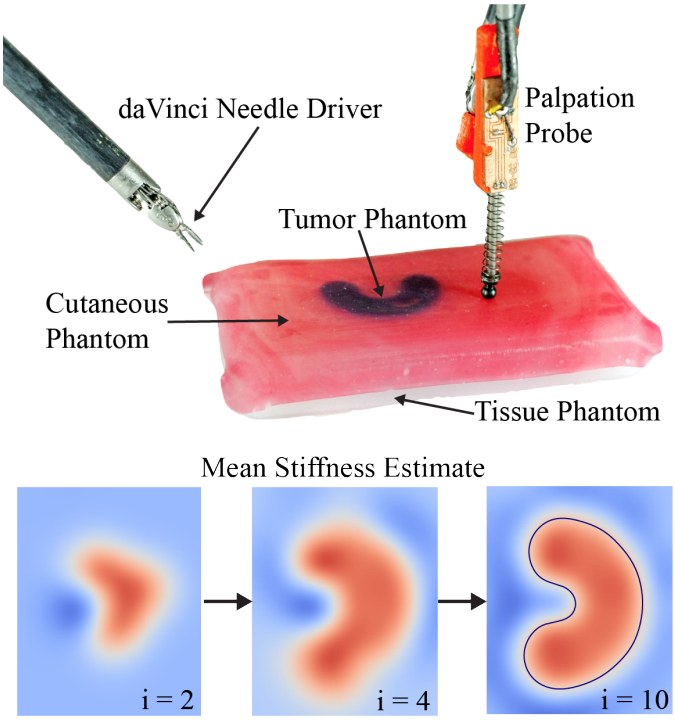

Figure 3.4: This figure illustrates autonomous localization of an embedded tumor in a tissue phantom. The top image shows the experimental setup with a palpation probe mounted on a Da Vinci Research Kit (dVRK). The sequence of images on the bottom illustrates the progression of the estimated stiffness over the tissue surface at intermediate stages (i=2, 4) and also the final estimate (i=10), with the estimated tumor boundary shown as a black line.

Soft Tissue Phantoms

Tumor phantoms were molded from silicone rubber (thickness 4.5 mm; Shore hardness 30A), and are embedded in softer silicon rubber *Ecoflex 00-20* (*Smooth-On*) with a total size of $100 \times 50 \times 20$ mm ($L \times W \times H$) simulating subcutaneous tissue. More details on phantom prepartion are described in Section 2.3.1.

Tumor Localization

We demonstrate the performance of tumor localization using the ILS-UCB algorithm, which outperformed other methods in simulation in terms of robustness to noise. We perform the localization experiment on a circular disk and a horseshoe-shaped tumor similar to the simulation setup. The search space is 5.4×4.9 cm ($26.46\,\text{cm}^2$) and the tumor areas are $3.84\,\text{cm}^2$ for the horseshoe and $1.84\,\text{cm}^2$ for the circle.

In these physical experiments, we use 16 samples on a uniform grid across the workspace to initialize the Gaussian process representation. Each tumor localization trial is run for at most 20 iterations with a batch of 10 measurements each iteration. Hence for each trial, 200 points are selected for measurement. Selected points were ordered by approximately solving a Travelling Salesman Problem at each iteration. In the interest of reducing computation time, scanning trajectories on the robot were computed by linearly interpolating between the points selected based on the sampling criterion.

At each iteration, the probe moves on the surface between the selected points, continuously collecting measurements. The robot moves at 5mm/s and measurements are collected at 1 sam-

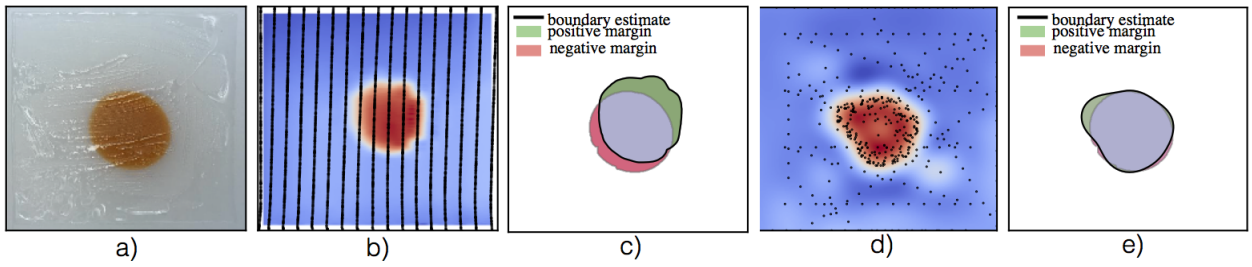

(i) Physical Experiments with a Circular Tumor

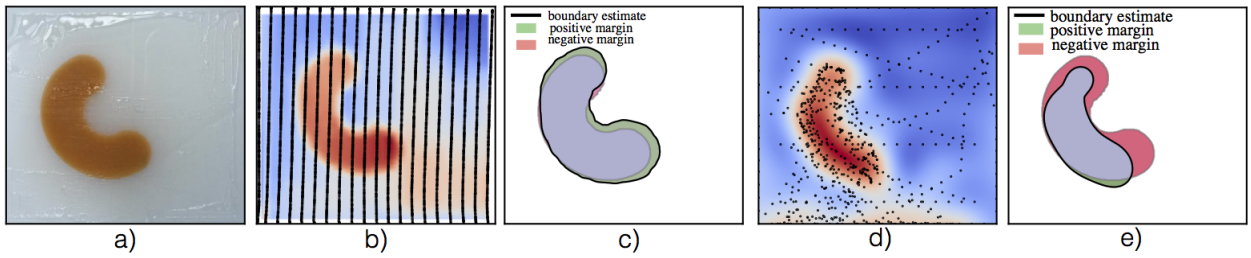

(ii) Physical Experiments with a Horse-Shoe Tumor

Figure 3.5: Physical Experiments: Tumor boundary estimation for a circular tumor phantom and a horseshoe-shaped tumor phantom with the PALP probe mounted on the dVRK. In both Figures (i) and (ii), (a) shows a top-down view of a molded rubberized tumor (orange) embedded in a silicone matrix (white). (b) shows the estimated stiffness map and the measurement locations for the raster scan (black). (c) shows the estimated boundary (black), with the error shown as positive and negative margins for the raster scan. (d) shows the estimated stiffness map measurement locations using ILS-UCB (black), and (e) shows the estimated boundary using ILS-UCB. Raster scanning for circular tumor takes 9,965 measurements and results in an error of 0.95 cm^2 from Ground Truth. While raster scanning in case of horseshoe-shaped tumor takes 11,774 measurements and results in an error of 0.98 cm^2 from Ground Truth. ILS-UCB takes 200 measurements both cases and results in an error of 1.51 cm^2 for the circular tumor and 0.24 cm^2 for the horseshoe-shaped tumor. It is worth noting that because ILS-UCB prioritizes sampling along an implicit level set of the stiffness, the measurements in (d) are clustered near the boundary of the tumor, resulting in faster convergence.

ple/mm. Unlike simulation experiments, measurements obtained between the selected points were incorporated into the GP update in physical experiments to speed up convergence.

To establish a baseline, we also perform a continuous raster scan using the robot the same speed with 2.0 mm between rows and obtaining $9,965$ measurements for the circle and $11,774$ measurements for the horseshoe. Table 3.2 details the results from raster scan as well as 5 trials of ILS-UCB on both the circular and horseshoe tumor. As in simulation, the values are the symmetric difference between estimated boundary and ground truth. Ground truth of the tumor boundaries is calculated by registering the search area between the camera image and the robot. The resulting image is then rectified and the tumor is segmented and the area is calculated from the resulting closed contour.

Table 3.2: Physical Experiments: Symmetric difference of the Ground Truth from the boundary estimate obtained from Raster Scans and ILS-UCB Adaptive Sampling algorithm. We use two tumor shapes, a circular disk-shaped tumor (#1) and a horse-shoe shaped tumor (#2) similar to the Simulation setup. The error is reported as a percentage of the search space area (26.46 cm^2). Raster scan uses approximately 10,000 samples and ILS-UCB uses 200 samples(20 iterations with a batch size of 10). ILS-UCB algorithm achieves the same order of performance with $10x$ fewer samples than Raster scan.

	Tumor#1 Circular Disk	Tumor#2 Horse-shoe
Raster Scan	3.60	3.73
ILS-UCB		
Trial 1	0.92	5.73
Trial 2	2.99	5.68
Trial 3	3.48	6.67
Trial 4	1.01	7.08
Trial 5	0.97	8.65
Mean	**1.87±1.25**	**6.76±1.21**

Figures 3.5ia-c and 3.5iia-c show the physical phantom, the raster scan path, and the estimate of the mean stiffness obtained using the raster scanning strategy. Figures 3.5id-e and 3.5iid-e show the estimate of the mean stiffness obtained after 20 iterations (in batches of 10) using ILS-UCB as the palpation algorithm for the two sets of physical experiments. Estimates of the boundary, as well as the positive and negative margins, are shown for Figures 3.5ie and 3.5iie. We use the 70% level set of the estimated stiffness map as the tumor boundary ($\alpha = 0.7$) which is indicated as a black line on the image. Note that because ILS-UCB prioritizes sampling along an implicit level set of the stiffness, the measurements in both Figures 3.5id and 3.5iid are clustered near the boundary of the tumor, resulting in faster convergence.

Chapter 4

Future Work and Conclusion

Review of Contributions

The main contributions of this thesis are hardware design for a novel low-cost, single-use palpation probe and bayesian algorithm using Gaussian Process Adaptive Sampling for tumor localization in Robot-assisted minimally invasive surgery (RMIS). In Chapter 2, we described the design of the low-cost, single-use palpation probe (PALP) for localizing subcutaneous blood vessels and tumors in RMIS. It senses relative differences in probe tip reaction force by measuring tip deflection with respect to a known spring constant using a Hall Effect sensor. The palpation probe fits on the end of a 8 mm diameter needle driver and extends it by 75 mm. The issue of sterilization is circumvented by use of disposable sensors, wherein a cost of less than $10 is achieved by use of off-the-shelf electronics and 3D printed components. The probe can be used for quasi-static sliding palpation as well as for discrete point palpation. We have used quasi-static sliding to localize subcutaneous blood vessel phantoms in silicone tissue.

The deflection response on sensor probe was characterized on a CNC machine tool with respect to various parameter settings such as multiple diameters of subcutaneous silicone cylinders (1.58-4.75 mm) at varying subcutaneous depths (1-5 mm) with a range of indentation depths (0-8 mm) and sliding speeds (0.5-21 mm/s). The probe can detect subcutaneous structures in phantoms of diameter 2.25 mm at a depth of up to 5 mm below the tissue surface and can operate up to speeds of 21 mm/s in sliding palpation. Experiments with the dVRK under autonomous execution demonstrate the feasibility of operation with the da Vinci.

In Chapter 3, we study tumor boundary estimation for robot-assisted minimally invasive surgery. We propose a Gaussian Process Adaptive Sampling algorithm, ILS-UCB, for autonomous tumor localization using palpation along implicit curves defined by stiffness measurements. Simulation results show that ILS-UCB can achieve up to a *10x* reduction in boundary estimation error over other methods. We also perform physical experiments, using the custom palpation probe we designed, on a da Vinci Research kit (dVRK) and observe that algorithmic search along implicit curves requires at least $10x$ fewer measurements than uniform raster scanning.

Limitations and Future Work

Design of Palpation Probe

The proposed sensor is primarily aimed to differentiate areas of interest based on relative deflection changes. We note that the sensor is limited to finding subcutaneous cylindrical phantoms up to 5mm. Methods for noise reduction and signal amplification can extend the limits of the sensor to identify deeper inclusions while negating the effects of errors in robot positioning.

Further, prior studies have not investigated methods for automated shape and impedance exploration in unknown flexible environments with a continuous probing mechanism. Possessing prior knowledge of the surface profile, the insertion axis of the dVRK could be used to maintain consistent probe-tip indentation depth across non-planar (or irregular) surface paths while searching tissue for inclusions.

And lastly, we will explore further miniaturization of the sensor. The electronics board can be miniaturized further to fit within the cylindrical profile of the da Vinci's 8 mm Needle Driver by designing with smaller surface mount components and traces. Improvement in design of the probe tip mount on the tool to allow for wrist rotation to control sensor orientation is also envisioned.

Gaussian Process Adaptive Sampling

A limitation of the proposed adaptive sampling method for tumor localization is that an accurate estimate of the surface geometry is required for a correct estimate of sub-surface stiffness and, by extension, of the tumor boundary. We show in Figure 3.2(c) that stiffness estimates are affected by errors in surface estimates. While using contact-based tactile probes such as *PALP*, controlling the applied force is critical in interpreting measurements, in addition to maintaining a constant indentation and performing measurements along surface normals. We will focus future effort on extending the current approach to non-planar surfaces with uncertain surface estimates using, e.g., a heteroscedastic GP model to model non-uniform measurement noise.

Automation of subcutaneous tumor excision in robot-assisted surgery is an important problem. Our recent work for Hamlyn Surgical Robotics Challenge [58] built a system for 2D cutting and tumor excision from planar phantoms. We will explore the use of PALP to localize subcutaneous inclusions for autonomous tumor excision in 3D.

Concluding Remarks

This thesis is a step towards closely examining the design of sensors and algorithms for high impact applications such as robot-assisted surgery. Tumor localization results presented in this thesis that couple the customized palpation probe PALP and Gaussian process adaptive sampling algorithms illustrate a new paradigm of low-cost yet effective design of autonomous system achieved through the interaction of design and optimization.

Bibliography

[1] S. A. Darzi and Y. Munz. "The Impact of Minimally Invasive Surgical Techniques". In: *Annu Rev Med.* Vol. 55. 2004, pp. 223–237 (cit. on p. 1).

[2] Ruben Veldkamp, Esther Kuhry, WC Hop, J Jeekel, G Kazemier, H Jaap Bonjer, Eva Haglind, L Pahlman, Miguel A Cuesta, Simon Msika, et al. "Laparoscopic surgery versus open surgery for colon cancer: short-term outcomes of a randomised trial". In: *Lancet Oncol* 6.7 (2005), pp. 477–484 (cit. on p. 1).

[3] Sudhakar K Venkatesh, Meng Yin, James F Glockner, Naoki Takahashi, Philip A Araoz, Jayant A Talwalkar, and Richard L Ehman. "Magnetic resonance elastography of liver tumors-preliminary results". In: *AJR. American Journal of Roentgenology* 190.6 (2008), p. 1534 (cit. on p. 1).

[4] J. Konstantinova, A. Jiang, K. Althoefer, P. Dasgupta, and T. Nanayakkara. "Implementation of Tactile Sensing for Palpation in Robot-Assisted Minimally Invasive Surgery: A Review". In: *Sensors Journal, IEEE* 14.8 (Aug. 2014), pp. 2490–2501 (cit. on pp. 1, 3–5).

[5] Kenoki Ohuchida and Makoto Hashizume. "Robotic surgery for cancer". In: *The Cancer Journal* 19.2 (2013), pp. 130–132 (cit. on p. 1).

[6] B Demi, Tobias Ortmaier, and Ulrich Seibold. "The touch and feel in minimally invasive surgery". In: *Haptic Audio Visual Environments and their Applications, 2005. IEEE International Workshop on*. IEEE. 2005, 6–pp (cit. on p. 1).

[7] Stephen B Williams, Ming-Hui Chen, Anthony V D'Amico, Aaron C Weinberg, Ravi Kacker, Michelle S Hirsch, Jerome P Richie, and Jim C Hu. "Radical retropubic prostatectomy and robotic-assisted laparoscopic prostatectomy: likelihood of positive surgical margin (s)". In: *Urology* 76.5 (2010), pp. 1097–1101 (cit. on p. 1).

[8] *ST79-Comprehensive guide to steam sterilization and sterility assurance in health care facilities,* ANSI/AAMI (cit. on pp. 1, 4).

[9] Stephen McKinley, Animesh Garg, Siddarth Sen, David V. Gealy, Jonathan P. McKinley, Yiming Jen, Menglung Luo, Doug Boyd, and Ken Goldberg. "An Interchangeable Surgical Instrument System with Application to Supervised Automation of Multilateral Tumor Resection." In: *IEEE Conf. on Automation Science and Engineering (CASE)*. 2016 (cit. on p. 2).

[10] Stephen McKinley, Animesh Garg, Siddarth Sen, Rishi Kapadia, Adithyavairavan Murali, Kirk Nichols, Susan Lim, Sachin Patil, Pieter Abbeel, Allison M Okamura, and Ken Goldberg. "A disposable haptic palpation probe for locating subcutaneous blood vessels in robot-assisted minimally invasive surgery". In: *IEEE Conf. on Automation Science and Engineering (CASE)*. 2015 (cit. on pp. 2, 20).

[11] Z Zhang, A.S Munawar, and G.S. Fischer. "Implementation of a Motion Planning Framework for the da Vinci Surgical System Research Kit (dVRK)". In: *Hamlyn Symposium on Medical Robotics (HSMR)*. 2014 (cit. on p. 3).

[12] Animesh Garg, Siddarth Sen, Rishi Kapadia, Yiming Jen, Stephen McKinley, Lauren Miller, and Ken Goldberg. "Tumor Localization using Automated Palpation with Gaussian Process Adaptive Sampling". In: *IEEE Conf. on Automation Science and Engineering (CASE)*. 2016 (cit. on p. 3).

[13] Mark R Cutkosky, Robert D Howe, and William R Provancher. "Force and tactile sensors". In: *Springer Handbook of Robotics*. Springer, 2008, pp. 455–476 (cit. on p. 3).

[14] Ana Luisa Trejos, J Jayender, M P Perri, M D Naish, R V Patel, and R A Malthaner. "Robot-Assisted Tactile Sensing for Minimally Invasive Tumor Localization". In: *The International Journal of Robotics Research* (2009). eprint: `http://ijr.sagepub.com/content/early/2009/05/19/0278364909101136.full.pdf+html` (cit. on p. 3).

[15] James C Gwilliam, Zachary Pezzementi, Erica Jantho, Allison M Okamura, and Steven Hsiao. "Human vs. robotic tactile sensing: Detecting lumps in soft tissue". In: *Haptics Symposium, 2010 IEEE*. IEEE. 2010, pp. 21–28 (cit. on p. 3).

[16] AP Sarvazyan. "Computerized palpation is more sensitive than human finger". In: *Proceedings of the 12th International Symposium on Biomedical Measurements and Instrumentation*. 1998, pp. 523–24 (cit. on p. 3).

[17] Pinyo Puangmali, Kaspar Althoefer, Lakmal D Seneviratne, Declan Murphy, and Prokar Dasgupta. "State-of-the-art in force and tactile sensing for minimally invasive surgery". In: *Sensors Journal, IEEE* 8.4 (2008), pp. 371–381 (cit. on pp. 3, 4).

[18] Pedro Silva Girão, Pedro Miguel Pinto Ramos, Octavian Postolache, and José Miguel Dias Pereira. "Tactile sensors for robotic applications". In: *Measurement* (2013) (cit. on p. 3).

[19] Mohsin I Tiwana, Stephen J Redmond, and Nigel H Lovell. "A review of tactile sensing technologies with applications in biomedical engineering". In: *Sensors and Actuators A: Physical* 179 (2012), pp. 17–31 (cit. on pp. 3, 4).

[20] Nobuyuki Futai, Kiyoshi Matsumoto, and Isao Shimoyama. "A flexible micromachined planar spiral inductor for use as an artificial tactile mechanoreceptor". In: *Sensors and Actuators A: Physical* 111.2 (2004), pp. 293–303 (cit. on p. 4).

[21] Chih-Chieh Wen and Weileun Fang. "Tuning the sensing range and sensitivity of three axes tactile sensors using the polymer composite membrane". In: *Sensors and Actuators A: Physical* 145 (2008), pp. 14–22 (cit. on p. 4).

[22] Hidekuni Takao, Kazuaki Sawada, and Makoto Ishida. "Monolithic silicon smart tactile image sensor with integrated strain sensor array on pneumatically swollen single-diaphragm structure". In: *Electron Devices, IEEE Transactions on* 53.5 (2006), pp. 1250–1259 (cit. on p. 4).

[23] A. Shashank, M.I. Tiwana, S.J. Redmond, and N.H. Lovell. "Design, simulation and fabrication of a low cost capacitive tactile shear sensor for a robotic hand". In: *Engineering in Medicine and Biology Society, 2009. EMBC 2009. Annual International Conference of the IEEE*. Sept. 2009, pp. 4132–4135 (cit. on p. 4).

[24] M.A. Qasaimeh, S. Sokhanvar, J. Dargahi, and M. Kahrizi. "PVDF-Based Microfabricated Tactile Sensor for Minimally Invasive Surgery". In: *Microelectromechanical Systems, Journal of* 18.1 (Feb. 2009), pp. 195–207 (cit. on p. 4).

[25] Yating Hu, R.B. Katragadda, Hongen Tu, Qinglong Zheng, Yuefa Li, and Yong Xu. "Bioinspired 3-D Tactile Sensor for Minimally Invasive Surgery". In: *Microelectromechanical Systems, Journal of* 19.6 (Dec. 2010), pp. 1400–1408 (cit. on p. 4).

[26] M. Ohka, N. Morisawa, H. Suzuki, J. Takata, H. Koboyashi, and H.B. Yussof. "A robotic finger equipped with an optical three-axis tactile sensor". In: *IEEE Int. Conf. on Robotics and Automation (ICRA)*. May 2008, pp. 3425–3430 (cit. on p. 4).

[27] S. Takenawa. "A soft three-axis tactile sensor based on electromagnetic induction". In: *Mechatronics, 2009. ICM 2009. IEEE International Conference on*. Apr. 2009, pp. 1–6 (cit. on p. 4).

[28] Damian McKay and Geoffrey Blake. "Optimum Incision Length for Port Insertion in Laparoscopic Surgery". In: *Annals of the Royal College of Surgeons of England* 88.1 (2006), p. 78 (cit. on pp. 4, 7).

[29] Mark P Ottensmeyer and J Kenneth Salisbury Jr. "In vivo data acquisition instrument for solid organ mechanical property measurement". In: *Medical Image Computing and Computer-Assisted Intervention–MICCAI 2001*. Springer. 2001, pp. 975–982 (cit. on p. 4).

[30] Kaspar Althoefer, Dinusha Zbyszewski, Hongbin Liu, Pinyo Puangmali, Lakmal Seneviratne, Benjamin Challacombe, Prokar Dasgupta, and Declan Murphy. "Air-cushion force sensitive probe for soft tissue investigation during minimally invasive surgery". In: *Sensors, 2008 IEEE*. IEEE. 2008, pp. 827–830 (cit. on p. 4).

[31] Yoshinobu Murayama, Mineyuki Haruta, Yuichi Hatakeyama, Takayuki Shiina, Hiroshi Sakuma, Seichi Takenoshita, Sadao Omata, and Christos E Constantinou. "Development of a new instrument for examination of stiffness in the breast using haptic sensor technology". In: *Sensors and Actuators A: Physical* 143.2 (2008), pp. 430–438 (cit. on p. 4).

[32] Marco Beccani, Christian Di Natali, Levin J Sliker, Jonathan A Schoen, Mark E Rentschler, and Pietro Valdastri. "Wireless tissue palpation for intraoperative detection of lumps in the soft tissue". In: *Biomedical Engineering, IEEE Trans. on* 61.2 (2014), pp. 353–361 (cit. on p. 4).

[33] Peng Peng and Rajesh Rajamani. "Handheld microtactile sensor for elasticity measurement". In: *Sensors Journal, IEEE* 11.9 (2011), pp. 1935–1942 (cit. on p. 4).

[34] Joshua B Gafford, Samuel B Kesner, Alperen Degirmenci, Robert J Wood, Robert D Howe, and Conor J Walsh. "A monolithic approach to fabricating low-cost, millimeter-scale multi-axis force sensors for minimally-invasive surgery". In: *IEEE Int. Conf. on Robotics and Automation (ICRA)*. IEEE. 2014, pp. 1419–1425 (cit. on p. 4).

[35] Hongbin Liu, David P Noonan, Benjamin J Challacombe, Prokar Dasgupta, Lakmal D Seneviratne, and Kaspar Althoefer. "Rolling mechanical imaging for tissue abnormality localization during minimally invasive surgery". In: *Biomedical Engineering, IEEE Transactions on* 57.2 (2010), pp. 404–414 (cit. on p. 4).

[36] Hongbin Liu, Jichun Li, Xiaojing Song, Lakmal D Seneviratne, and Kasparl Althoefer. "Rolling indentation probe for tissue abnormality identification during minimally invasive surgery". In: *Robotics, IEEE Transactions on* 27.3 (2011), pp. 450–460 (cit. on p. 4).

[37] Greig L McCreery, Ana Luisa Trejos, Michael D Naish, Rajni V Patel, and Richard A Malthaner. "Feasibility of locating tumours in lung via kinaesthetic feedback". In: *The International Journal of Medical Robotics and Computer Assisted Surgery* 4.1 (2008), pp. 58–68 (cit. on p. 4).

[38] Adam M Zysk, Freddy T Nguyen, Amy L Oldenburg, Daniel L Marks, and Stephen A Boppart. "Optical coherence tomography: a review of clinical development from bench to bedside". In: *Journal of Biomedical Optics* 12.5 (2007), pp. 051403–051403 (cit. on p. 4).

[39] Paul Hebert, Thomas Howard, Nicolas Hudson, Jiaxin Ma, and Joel W Burdick. "The next best touch for model-based localization". In: *IEEE Int. Conf. on Robotics and Automation (ICRA)*. 2013 (cit. on p. 5).

[40] Mats Bjorkman, Yasemin Bekiroglu, Virgile Hogman, and Danica Kragic. "Enhancing visual perception of shape through tactile glances". In: *IEEE Int. Conf. on Intelligent Robots and Systems (IROS)*. 2013 (cit. on p. 5).

[41] Stanimir Dragiev, Marc Toussaint, and Michael Gienger. "Uncertainty aware grasping and tactile exploration". In: *IEEE Int. Conf. on Robotics and Automation (ICRA)*. 2013 (cit. on p. 5).

[42] Geoffrey A Hollinger, Brendan Englot, Franz S Hover, Urbashi Mitra, and Gaurav S Sukhatme. "Active planning for underwater inspection and the benefit of adaptivity". In: *International Journal of Robotics Research* (2012) (cit. on p. 5).

[43] Roger E Goldman, Andrea Bajo, and Nabil Simaan. "Algorithms for autonomous exploration and estimation in compliant environments". In: *Robotica* 31.01 (2013), pp. 71–87 (cit. on p. 6).

[44] Kirk Nichols and Allison M Okamura. "Methods to Segment Hard Inclusions in Soft Tissue During Autonomous Robotic Palpation". In: *IEEE Trans. on Robotics* 31.2 (2015), pp. 344–354 (cit. on p. 6).

[45] E. Ayvali, R. A. Srivatsan, L. Wang, R. Roy, N. Simaan, and H. Choset. "Using Bayesian Optimization to Guide Probing of a Flexible Environment for Simultaneous Registration and Stiffness Mapping". In: *IEEE Int. Conf. on Robotics and Automation (ICRA)*. 2016 (cit. on p. 6).

[46] Alkis Gotovos, Nathalie Casati, Gregory Hitz, and Andreas Krause. "Active learning for level set estimation". In: *IJCAI*. 2013 (cit. on pp. 6, 18).

[47] G. Hitz, A. Gotovos, F. Pomerleau, M.-E. Garneau, C. Pradalier, A. Krause, and R.Y. Siegwart. "Fully autonomous focused exploration for robotic environmental monitoring". In: *IEEE Int. Conf. on Robotics and Automation (ICRA)*. May 2014 (cit. on p. 6).

[48] P. Chalasani, L. Wang, R. Roy, N. Simaan, R. H. Taylor, and M. Kobilarov. "Concurrent nonparametric estimation of organ geometry and tissue stiffness using continuous adaptive palpation". In: *IEEE Int. Conf. on Robotics and Automation (ICRA)*. 2016 (cit. on p. 6).

[49] R. A. Srivatsan, E. Ayvali, L. Wang, R. Roy, N. Simaan, and H. Choset. "Complementary model update: A method for simultaneous registration and stiffness mapping in flexible environments". In: *IEEE Int. Conf. on Robotics and Automation (ICRA)*. 2016 (cit. on p. 6).

[50] Carl Edward Rasmussen. "Gaussian processes for machine learning". In: MIT Press, 2006 (cit. on p. 17).

[51] Stanimir Dragiev, Marc Toussaint, and Michael Gienger. "Re-grasping for Gaussian Process Implicit Surface". In: *IEEE ICRA Workshop on Autonomous Grasping*. 2014 (cit. on p. 18).

[52] Stanimir Dragiev, Marc Toussaint, and Michael Gienger. “Gaussian Process Implicit Surfaces for shape estimation and grasping”. In: *IEEE Int. Conf. on Robotics and Automation (ICRA)*. 2011 (cit. on p. 18).

[53] Jeffrey Mahler, Sachin Patil, Ben Kehoe, Jur van den Berg, Matei Ciocarlie, Pieter Abbeel, and Ken Goldberg. “GP-GPIS-OPT: Grasp planning with shape uncertainty using Gaussian process implicit surfaces and Sequential Convex Programming”. In: *IEEE Int. Conf. on Robotics and Automation (ICRA)*. 2015 (cit. on p. 18).

[54] The GPy authors. *GPy: A Gaussian process framework in python*. `http://github.com/SheffieldML/GPy`. 2012–2015 (cit. on p. 20).

[55] A. Murali, S. Sen, B. Kehoe, A. Garg, S. McFarland, S. Patil, W.D. Boyd, S. Lim, P. Abbeel, and K. Goldberg. “Learning by Observation for Surgical Subtasks: Multilateral Cutting of 3D Viscoelastic and 2D Orthotropic Tissue Phantoms”. In: *IEEE Int. Conf. on Robotics and Automation (ICRA)*. 2015 (cit. on p. 22).

[56] S. Sen, A. Garg, D. V. Gealy, S. McKinley, Y. Jen, and K. Goldberg. “Automating Multiple-Throw Multilateral Surgical Suturing with a Mechanical Needle Guide and Sequential Convex Optimization”. In: *IEEE Int. Conf. on Robotics and Automation (ICRA)*. 2016 (cit. on p. 22).

[57] P Kazanzides, Z Chen, A Deguet, G.S. Fischer, R.H. Taylor, and S.P. DiMaio. “An Open-Source Research Kit for the da Vinci Surgical System”. In: *IEEE Int. Conf. on Robotics and Automation (ICRA)*. 2014 (cit. on p. 22).

[58] Stephen McKinley, Siddarth Sen, Animesh Garg, Yiming Jen, David Gealy, Pieter Abbeel, and Ken Goldberg. *Autonomous Tumor Localization and Extraction: Palpation, Incision, Debridement and Adhesive Closure with the da Vinci Research Kit*. Hamlyn Surgical Robotics Conference, London. June 2015 (cit. on p. 27).